Aalborg Universitet

AALBORG UNIVERSITY

Sensorless Control of Brushless Doubly Fed Induction Machine Using a Control Winding Current MRAS Observer

Yang, Jian; Tang, Weiyi; Zhang, Guanguan; Sun, Yao; Ademi, Sul; Blaabjerg, Frede; Zhu, Qi

Published in:
I E E E Transactions on Industrial Electronics

DOI (link to publication from Publisher):
10.1109/TIE.2018.2831168

Publication date:
2019

Document Version
Accepted author manuscript, peer reviewed version

Link to publication from Aalborg University

Citation for published version (APA):
Yang, J., Tang, W., Zhang, G., Sun, Y., Ademi, S., Blaabjerg, F., & Zhu, Q. (2019). Sensorless Control of Brushless Doubly Fed Induction Machine Using a Control Winding Current MRAS Observer. *I E E E Transactions on Industrial Electronics*, *66*(1), 728 - 738. Article 8352049. https://doi.org/10.1109/TIE.2018.2831168

General rights
Copyright and moral rights for the publications made accessible in the public portal are retained by the authors and/or other copyright owners and it is a condition of accessing publications that users recognise and abide by the legal requirements associated with these rights.

- Users may download and print one copy of any publication from the public portal for the purpose of private study or research.
- You may not further distribute the material or use it for any profit-making activity or commercial gain
- You may freely distribute the URL identifying the publication in the public portal -

Take down policy
If you believe that this document breaches copyright please contact us at vbn@aub.aau.dk providing details, and we will remove access to the work immediately and investigate your claim.

Downloaded from vbn.aau.dk on: December 04, 2025

This article has been accepted for publication in a future issue of this journal, but has not been fully edited. Content may change prior to final publication. Citation information: DOI 10.1109/TIE.2018.2831168, IEEE Transactions on Industrial Electronics

Sensorless Control of Brushless Doubly-Fed Induction Machine Using a Control Winding Current MRAS Observer

Jian Yang, *Member*, *IEEE*, Weiyi Tang, Guanguan Zhang, Yao Sun, *Member*, *IEEE*, Sul Ademi, *Member*, *IEEE*, Frede Blaabjerg, *Fellow*, *IEEE* and Qi Zhu

***Abstract*—In order to realize sensorless control for brushless doubly-fed induction machine (BDFIM), this paper presents a model reference adaptive system (MRAS) observer, designed based on the error of the control winding current. Furthermore, a phase-locked loop (PLL) is employed to estimate the current winding position and rotor speed. Consequently, a detailed theoretical derivation proves that the MRAS observer is stable and the dynamic performance is good. Thus, it does not cause any estimated speed error in steady state. Moreover, the estimated position error is bounded and trivial, thus its effects on the sensorless control of the BDFIM are neglected. The correctness, feasibility, and robustness of the proposed sensorless control method are verified by means of experimental validation on a 30kW test rig.**

***Index Terms*—Brushless doubly-fed induction machines, model reference adaptive system observer, sensorless control, angular velocity control.**

NOMENCLATURE

v, i, ψ	Voltage, current and flux
R, L	Resistance and self-inductance
L_{hp}	Coupling inductance between power winding (PW) and rotor
L_{hc}	Coupling inductance between control winding (CW) and rotor
τ_e, τ_L	Electromagnetic torque and load torque
P	Number of pole pairs
ω_r	Rotor mechanical angular speed
ω_p	Electrical angular speed of the grid
θ_r, θ_p	Angular positions of rotor and PW flux frame
$\mathbf{N}$, $\|\mathbf{N}\|$	Arbitrary matrix and its l_2-norm
x	Electrical variables of the motor
γ	Rotor position
Ref	Reference
Subscripts	
p, c, r	PW, CW, rotor
a b, c	Windings a, b and c
Superscripts	
d, q	Synchronous rotating reference frames
$\alpha\beta p$, $\alpha\beta c$	Stationary reference frames of PW and CW
$\alpha\beta r1$, $\alpha\beta r2$	Stationary reference frames of the rotor in a P_p and P_c pole-pair-type distributions.
*	Complex conjugate
^	Estimated value
~	Estimation error between the nominal value and the estimated value

Manuscript received August 18, 2017; revised November 20, 2017 and January 23, 2018; accepted April 10, 2018. This work was supported in part by the National Natural Science Foundation of China under Grant 51777217, and the Project of Innovation-Driven Plan in the Central South University. Corresponding Author: Guanguan Zhang.

Jian Yang, Weiyi Tang, Guanguan Zhang, Yao Sun and Qi Zhu are with the School of Information Science and Engineering, Central South University, Changsha 410083, China (e-mail: jian.yang@csu.edu.cn; 154601016@csu.edu.cn; dr_zgg@163.com; yaosuncsu@gmail.com; csu_zhuqi@163.com).

Sul Ademi is with the Warwick Manufacturing Group (WMG), University of Warwick, Coventry, U.K. (e-mail: s.ademi@warwick.ac.uk).

Frede Blaabjerg is with the Department of Energy Technology, Aalborg University, Aalborg DK-9220, Denmark (e-mail: fbl@et.aau.dk).

I. INTRODUCTION

The brushless doubly-fed machines (BDFMs) inherit advantages of the doubly-fed induction generator (DFIG), of which the converter is generally about one-third of the generator rating for limited speed range applications. Furthermore, BDFM does not need the slip ring hence it is free of DFIG's drawbacks, thus enhances system reliability due to the brushless rotor topology, showing their promising perspective in variable speed drive [1], and generating application [2], [3]. Usually, the coordinate orientation is essential for the BDFM control, such as the vector control, and speed sensors since quadrature encoders are utilized to measure angular velocity, however, the utilization of speed sensors increases system costs, maintenance difficulties and reduces the system reliability. Therefore, sensorless control of BDFMs warrants further investigation, especially when BDFMs are exposed and operated under harsh conditions. The BDFM comprises of two stator windings (PW and CW), the PW is grid-connected, while the CW is connected via back-to-back converter system as depicted in Fig. 1. There are two BDFMs rotor types, namely brushless doubly-fed induction machine (BDFIM) classified as wound-rotor/nested-loop-cage type [4]-[6], or reluctance type denoted as brushless doubly-fed reluctance generator (BDFRG) [7], [8].

A number of sensorless control methods have been investigated in the DFIG and BDFRG case. In respect to the

0278-0046 (c) 2018 IEEE. Personal use is permitted, but republication/redistribution requires IEEE permission. See http://www.ieee.org/publications_standards/publications/rights/index.html for more information.

This article has been accepted for publication in a future issue of this journal, but has not been fully edited. Content may change prior to final publication. Citation information: DOI 10.1109/TIE.2018.2831168, IEEE Transactions on Industrial Electronics

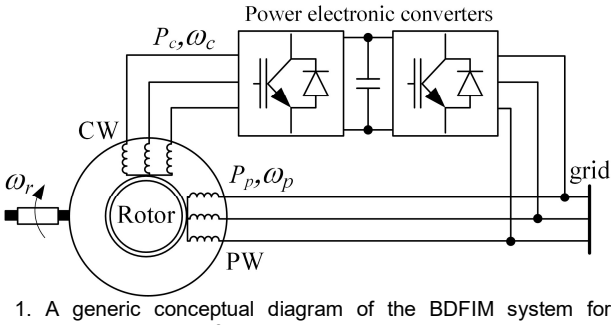

Fig. 1. A generic conceptual diagram of the BDFIM system for adjustable speed constant frequency grid-connected applications.

DFIG, previous studies have investigated several model reference adaptive system (MRAS) observer based methods, evolving around error variables such as stator/rotor currents along with stator/rotor flux, making them suitable for stand-alone and grid-connected operations [9]-[11]. The effects of mismatched parameters on the performances of sensorless control of DFIGs based on MRAS observers are analyzed in [12], while an adaptive tuning of the stator inductance in a rotor current-based MRAS observer is introduced in [13]. With respect to the BDFRG, the sensorless operation using model-based methods are presented in [14]. The sensorless speed field (flux) oriented control strategy in [15] eliminates the variable switching frequency and flux (torque) ripple problems, which acts as a benchmark and lays the foundations for the sensorless control of the BDFIMs. The BDFIMs lag behind its slip-ring counterparts, which could be down to the model complexities and heavy parameter dependence.

However, due to the special physical rotor structure, the BDFIM consists of the different mathematical model compared with the DFIG or BDFRG [7], [16], thus the common sensorless control methods cannot be directly applied to the BDFIM, hence their feasibility should be verified.

To the best of the authors' knowledge, studies of the sensorless control of the BDFIM of such nature are rare except for [17], whereby effectiveness of the MRAS observer for sensorless control of the BDFIM is verified by neglecting the rotor resistance of the BDFIM, but details of the theoretical derivation and design approaches are not discussed. Since the inherent existence of the rotor resistance, the analyses are also not sufficient and complete. Therefore, the studies in this paper aim to cater and address these requirements of sensorless control of BDFIM. This paper focuses on the design and analyses of the sensorless controller of BDFIM and details the design process of MRAS observer based on the CW current model, so are the stability, dynamic and steady-state performance of the sensorless controller.

The main contributions of the paper are systematically evaluated as follows:

1) A MRAS observer for the sensorless control of the BDFIM is proposed based on the control winding current model.

2) The stability, uncertainties toward parameter variations, the dynamic and steady-state performance of the proposed MRAS observer are thoroughly analyzed. The qualitative and quantitative approaches illustrate that MRAS observer is stable and its dynamic performance is good, while showing robustness to uncertainties in parameter variations. Moreover, the results show that the corresponding estimated position error is trivial and has little effect on the vector control of the BDFIM.

This paper is organized as follows. The system configuration and mathematical model of the BDFIM are constructed in Section II. The design and development of control winding current-based MRAS observer are evaluated. The local/global stability, dynamic and steady-state performance are developed while upper bound of the estimated error and the parameter sensitivity analysis are outlined in Section III. Experimental setup/results and discussions are presented in Section IV. Finally, conclusions have been drawn.

II. System Configuration and Mathematical Model of the BDFIM

The wound-type rotor of the BDFIMs [5] is functionally equivalent to cascaded doubly-fed induction machine (CDFIM) [18], [19] with the assumption of the negligible saturation, uniform airgap, and sinusoidal distributed stator windings. The only configuration which gives satisfying results is the inverse interconnections of rotor windings [18], which means that $i_r^{\alpha\beta r1} = -i_r^{\alpha\beta r2*}$. With a special nested cage structure, the cage-type rotor of BDFIMs have analogues rotor current properties above, and their derived mathematical models of the wound-type and cage-type rotor are the same [20]. Thus, the proposed sensorless controller can be applied to both BDFIM types. Without loss of generality, the rotor type of the BDFIM used in this paper for experimental verification is the wound-rotor type. There are two fundamental magnetic fields in the BDFIMs, with four stationary reference frame, *αβp*, *αβc*, *αβr1*, and *αβr2*, as shown in Fig. 2. δ_1 is the initial angular position between *αβr1* and *αβp,* while δ_2 is the initial angular position *αβr2* and *αβc.* The modeling of BDFIM has been discussed and detailed in [20], [21], therefore it is omitted here.

The BDFIM mathematical model in stationary frame is given as

$$v_p^{\alpha\beta p} = R_p i_p^{\alpha\beta p} + d\psi_p^{\alpha\beta p} \big/ dt \tag{1}$$

$$\psi_p^{\alpha\beta p} = L_p i_p^{\alpha\beta p} + L_{hp} e^{j\left(P_p\theta_r + \delta_1\right)} i_r^{\alpha\beta r1} \tag{2}$$

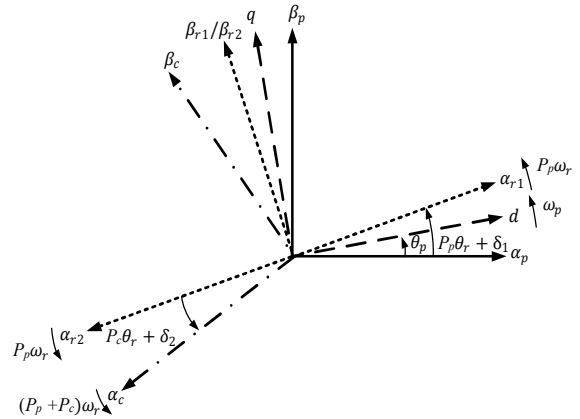

Fig. 2. Stationary reference frames of the BDFIM configuration.

0278-0046 (c) 2018 IEEE. Personal use is permitted, but republication/redistribution requires IEEE permission. See http://www.ieee.org/publications_standards/publications/rights/index.html for more information.

This article has been accepted for publication in a future issue of this journal, but has not been fully edited. Content may change prior to final publication. Citation information: DOI 10.1109/TIE.2018.2831168, IEEE Transactions on Industrial Electronics

$$v_c^{\alpha\beta c} = R_c i_c^{\alpha\beta c} + d\psi_c^{\alpha\beta c}/dt \quad (3)$$

$$\psi_c^{\alpha\beta c} = L_c i_c^{\alpha\beta c} - L_{hc} e^{j(P_c\theta_r+\delta_2)} i_r^{\alpha\beta r1*} \quad (4)$$

$$0 = R_r i_r^{\alpha\beta r1} + d\psi_r^{\alpha\beta r1}/dt \quad (5)$$

$$\psi_r^{\alpha\beta r1} = L_r i_r^{\alpha\beta r1} + L_{hp} e^{-j\left(P_p\theta_r+\delta_1\right)} i_p^{\alpha\beta p} - L_{hc} e^{j(P_c\theta_r+\delta_2)} i_c^{\alpha\beta c*} \quad (6)$$

According to expressions (1)-(6), using Park transformation, the BDFIM model in the general synchronously rotating *d-q* reference frame used for the vector control is derived. The rotor current and rotor flux are $i_r^{dq} = e^{-j(\theta_p - P_p\theta_r - \delta_1)} i_r^{\alpha\beta r1}$ and $\psi_r^{dq} = e^{-j(\theta_p - P_p\theta_r - \delta_1)} \psi_r^{\alpha\beta r1}$, and the PW and CW variables are $x_p^{dq} = e^{-j\theta_p} x_p^{\alpha\beta p}$ and $x_c^{dq} = -e^{-j(\theta_p-\gamma)} x_c^{\alpha\beta c*}$, respectively. Thus, the BDFIM model is described as

$$v_p^{dq} = R_p i_p^{dq} + d\varphi_p^{dq}/dt + j\omega_p \varphi_p^{dq} \quad (7)$$

$$\psi_p^{dq} = L_p i_p^{dq} + L_{hp} i_r^{dq} \quad (8)$$

$$v_c^{dq} = R_c i_c^{dq} + d\psi_c^{dq}/dt + j(\omega_p - (P_p + P_c)\omega_r)\psi_c^{dq} \quad (9)$$

$$\psi_c^{dq} = L_c i_c^{dq} + L_{hc} i_r^{dq} \quad (10)$$

$$0 = R_r i_r^{dq} + d\psi_r^{dq}/dt + j(\omega_p - P_p\omega_r)\psi_r^{dq} \quad (11)$$

$$\psi_r^{dq} = L_r i_r^{dq} + L_{hp} i_p^{dq} + L_{hc} i_c^{dq} \quad (12)$$

The position angle γ and the rotor speed ω_r are written as

$$\gamma = P_p\theta_r + \delta_1 + P_c\theta_r + \delta_2 \quad (13)$$

$$\omega_r = d\theta_r/dt = (d\gamma/dt)/(P_p + P_c) \quad (14)$$

In the absence of speed sensor, γ and rotor speed ω_r are unknown and should be observed, in order to control the BDFIM using the vector control algorithm and realize the speed feedback control.

III. Sensorless Control Scheme Based on MRAS Observer

A. Sensorless MRAS Observer Framework

The MRAS observer makes use of the redundancy of two machine models termed as a reference model and adjustable model respectively with different structures that estimate the same state variable [22]. The general sensorless MRAS observer consists of the reference model and the adjustable model, which are constructed based on the three measured values $v_p^{\alpha\beta p}$, $i_p^{\alpha\beta p}$ and $i_c^{\alpha\beta c}$. An error signal ε is obtained by a cross-product of the two vectors generated by the reference model and adjustable model, and the estimated position angle $\hat{\gamma}$ is achieved from a phase locked loop (PLL) estimator.

Essentially, the PW current can also be used as the control state variable for the MRAS observer. However, when active and reactive power are controlled to be nearly zero on the PW side, the PW current is also nearly zero. In this case, the error obtained from the reference model and adjustable model of the PW current-based MRAS observer is not sensitive to the estimated position error. Different from the PW current, the CW current is always excited so that the CW current is used as the control state variable for the MRAS observer in this paper. Furthermore, the stability, dynamic and steady-state performance of the proposed observer are subsequently analyzed based on this general framework in part *B*, *C*, *D* and *E*, and the global stability of the MRAS observer is derived in part *F*.

B. Design of the MRAS Observer

In this paper, the state variable estimated by the two machine models is based on the CW current, and the schematic diagram of the control system is illustrated in Fig. 3. Since the CW current is measured, the reference model is easily obtained by transferring the measured current to the $\alpha\beta c$ reference frame.

Combining (2), (4), (5) and (6) yields the CW current described by the adjustable model as

$$i_c^{\alpha\beta c*} = i_{c1}^{\alpha\beta c*} + O(R_r) \quad (15)$$

where $i_{c1}^{\alpha\beta c*} = e^{-j\gamma}(L_r\psi_p^{\alpha\beta p} + (L_{hp}{}^2 - L_rL_p)i_p^{\alpha\beta p})/(L_{hp}L_{hc})$,

$O(R_r) = e^{-j(P_c\theta_r+\delta_2)} R_r \int\left(e^{-j\left(P_p\theta_r+\delta_1\right)}\left(\psi_p^{\alpha\beta p} - L_p i_p^{\alpha\beta p}\right)\right)dt \Big/ \left(L_{hc}L_{hp}\right)$

In order to obtain the estimated CW current, the adjustable model is constructed as

$$\hat{i}_c^{\alpha\beta c*} = \hat{i}_{c1}^{\alpha\beta c*} + \hat{O}(R_r) \quad (16)$$

where $\hat{i}_{c1}^{\alpha\beta c*} = e^{-j\hat{\gamma}}\left(L_r\psi_p^{\alpha\beta p} + \left(L_{hp}{}^2 - L_rL_p\right)i_p^{\alpha\beta p}\right)\Big/\left(L_{hp}L_{hc}\right)$,

$\psi_p^{\alpha\beta p} = \int(v_p^{\alpha\beta p} - R_p i_p^{\alpha\beta p})dt$ and $\hat{O}(R_r)$ is the estimation of

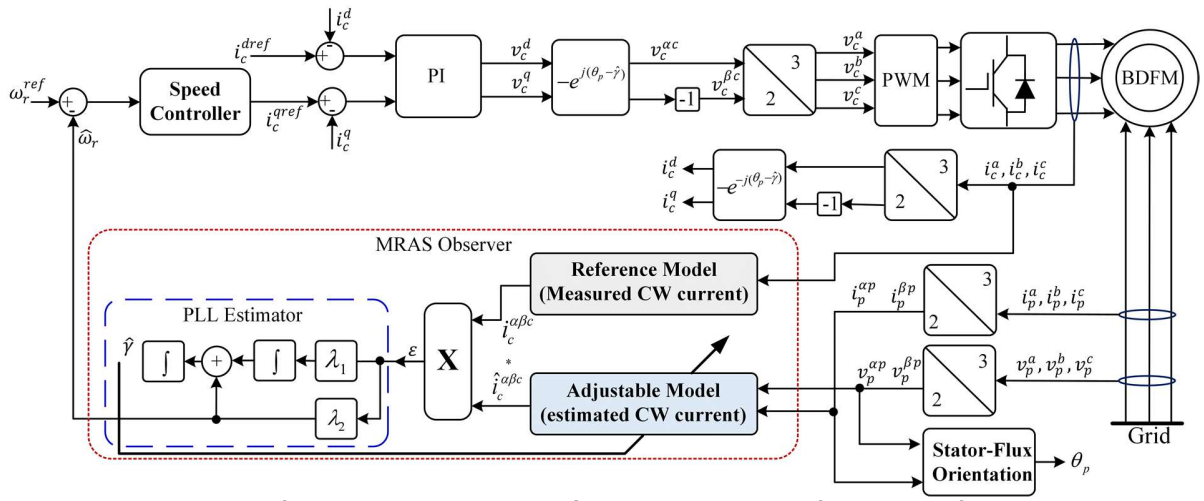

Fig. 3. A structural block diagram of the proposed sensorless MRAS observer control system for the inverter-fed BDFIM.

0278-0046 (c) 2018 IEEE. Personal use is permitted, but republication/redistribution requires IEEE permission. See http://www.ieee.org/publications_standards/publications/rights/index.html for more information.

This article has been accepted for publication in a future issue of this journal, but has not been fully edited. Content may change prior to final publication. Citation information: DOI 10.1109/TIE.2018.2831168, IEEE Transactions on Industrial Electronics

$O(R_r)$.

The scalar error signal is constructed as follow:

$$\varepsilon = \mathrm{Im}(\hat{i}_c^{\alpha\beta c*} i_c^{\alpha\beta c}) \tag{17}$$

By utilizing the algorithm in [22], the tuning signal $\hat{\gamma}$ is obtained through a PLL estimator from the scalar error signal:

$$d\hat{\gamma}/dt = \hat{\omega}_\gamma + \lambda_2 \varepsilon \tag{18}$$

$$d\hat{\omega}_\gamma/dt = \lambda_1 \varepsilon \tag{19}$$

where $\lambda_1 = \rho^2/k$, $\lambda_2 = 2\rho/k$, $k = \left\| i_c^{\alpha\beta c} \right\|_2 \left\| \hat{i}_c^{\alpha\beta c} \right\|_2$, and ρ is a constant and is designed in part E of this section.

The estimated rotor speed used for the speed control is

$$\hat{\omega}_r = \hat{\omega}_\gamma / \left(P_p + P_c \right) \tag{20}$$

C. Local Stability, Dynamic and Steady State Analyses of the MRAS observer

The main purpose of the sensorless control is to observe γ shown in (13) and the rotor speed of BDFIM. According to (15) and (16), the amplitudes of $i_{c1}^{\alpha\beta c*}$ and $\hat{i}_{c1}^{\alpha\beta c*}$ are equal, while the angle between these two vectors is $\tilde{\gamma} = \gamma - \hat{\gamma}$, and $\tilde{\gamma}$ is the estimated angle error. This is described as

$$\hat{i}_{c1}^{\alpha\beta c*} = i_{c1}^{\alpha\beta c*} e^{j\tilde{\gamma}} \tag{21}$$

Let $\Delta\theta_1$ is the angle error between $i_{c1}^{\alpha\beta c*}$ and $i_c^{\alpha\beta c*}$, $\Delta\theta_2$ is the angle error between $\hat{i}_{c1}^{\alpha\beta c*}$ and $\hat{i}_c^{\alpha\beta c*}$. They are illustrated as

$$i_{c1}^{\alpha\beta c*} = \left(\left\| i_{c1}^{\alpha\beta c*} \right\|_2 i_c^{\alpha\beta c*} e^{j\Delta\theta_1} \right) \Big/ \left\| i_c^{\alpha\beta c*} \right\|_2 \tag{22}$$

$$\hat{i}_{c1}^{\alpha\beta c*} = \left(\left\| \hat{i}_{c1}^{\alpha\beta c*} \right\|_2 \hat{i}_c^{\alpha\beta c*} e^{j\Delta\theta_2} \right) \Big/ \left\| \hat{i}_c^{\alpha\beta c*} \right\|_2 \tag{23}$$

Figure 4 shows the relationship between $i_c^{\alpha\beta c*}$, $i_{c1}^{\alpha\beta c*}$, $\hat{i}_{c1}^{\alpha\beta c*}$ and $\hat{i}_c^{\alpha\beta c*}$, when the MRAS observer is stable, the angle between the $\hat{i}_c^{\alpha\beta c*}$ and $i_c^{\alpha\beta c*}$ is zero, that is $\Delta\theta_1 + \Delta\theta_2 + \tilde{\gamma} = 0$. Here $\Delta\theta$ is defined as $\Delta\theta = \Delta\theta_1 + \Delta\theta_2$, $\tilde{\gamma} = -\Delta\theta$ in steady state as demonstrated in the following discussion. In this case, the estimated error is analyzed by calculating $\Delta\theta$ as shown in part *D*.

According to (5) and (6), CW current is

$$i_c^{\alpha\beta c*} = \left(L_r i_r^{\alpha\beta r1} + L_{hp} e^{-j\left(P_p\theta_r + \delta_1\right)} i_p^{\alpha\beta p} + \int \left(R_r i_r^{\alpha\beta r1} \right) dt \right) \Big/ \left(L_{hc} e^{j\left(P_c\theta_r + \delta_2\right)} \right) \tag{24}$$

According to (15) and (24), $O(R_r)$ can also be expressed as follows:

$$O(R_r) = \int \left(R_r i_r^{\alpha\beta r1} \right) dt \Big/ \left(L_{hc} e^{j\left(P_c\theta_r + \delta_2\right)} \right) \tag{25}$$

With Laplace transforms, (25) is transposed to the following alternative expression

$$O(R_r) = \left(R_r i_r^{\alpha\beta r1} \right) \Big/ \left(L_{hc} e^{\left(P_c\theta_r + \delta_2\right)} s \right) \tag{26}$$

Since the MRAS observer dynamics are much slower than the current dynamics, the rotor current converges to the steady-state solution within the time scale of the MRAS observer. Therefore, (26) is described as

$$O(R_r) = -\left(j e^{-j\left(P_c\theta_r + \delta_2\right)} i_r^{\alpha\beta r1} R_r \right) \Big/ \left(L_{hc} \omega_{slr} \right) \tag{27}$$

where $\omega_{slr} = \omega_p - P_p \omega_r$

On the basis of the controller design principle in the drive system, it is reasonable to assume that the current converges to steady state in the time scale of the MRAS observer, thus the amplitude of $i_c^{\alpha\beta c*}$ and $i_r^{\alpha\beta r1}$ are constant. Due to the slow time constant characteristics of the mechanical components, ω_{slr} is also constant in the time scale of the MRAS observer. Consequently, the amplitude of $O(R_r)$ is also constant according to (27). Meanwhile, in the stationary reference frame, since the rotating speed of $i_r^{\alpha\beta r1}$ is $P_p\omega_r$, the rotating speed of $O(R_r)$ is $(P_p + P_c)\omega_r$ according to (27), and it is identical to the rotating speed of $i_c^{\alpha\beta c*}$. It can be seen from (15) that the rotating speed of $i_{c1}^{\alpha\beta c*}$ is the same as that of $i_c^{\alpha\beta c*}$ in the stationary reference frame. As a result, $\Delta\theta_1$ (the angle error between $i_{c1}^{\alpha\beta c*}$ and $i_c^{\alpha\beta c*}$) is invariable.

The differential of $\Delta\theta_1$ is described as

$$d\Delta\theta_1/dt = 0 \tag{28}$$

Similarly, $\Delta\theta_2$ is designed as

$$d\Delta\theta_2/dt = 0 \tag{29}$$

The state space equation analysis is demonstrated as follows, where the stabilization of the sensorless observer is also proved.

According to (17), (21), (22) and (23), the scalar error signal can be constructed as

$$\varepsilon = \left\| i_c^{\alpha\beta c} \right\|_2 \left\| \hat{i}_c^{\alpha\beta c} \right\|_2 \sin(\tilde{\gamma} + \Delta\theta) \tag{30}$$

A new variable ω_γ is defined as a multiple of the rotor speed, which is represented as

$$\omega_\gamma = (P_p + P_c)\omega_r \tag{31}$$

If $\tilde{\gamma} + \Delta\theta$ is small, $\sin\left(\tilde{\gamma} + \Delta\theta\right)$ can be linearized as $\tilde{\gamma} + \Delta\theta$. The error ε will be derived as

$$\varepsilon = k(\tilde{\gamma} + \Delta\theta) \tag{32}$$

Assume that the rotor speed is constant in the time scale of the MRAS observer, then

$$d\omega_\gamma/dt = 0 \tag{33}$$

According to (13), (14) and (31), the differential of γ is

$$d\gamma/dt = \omega_\gamma \tag{34}$$

According to (18), (19), (28), (29) (32), (33) and (34), $\tilde{\omega}_\gamma = \omega_\gamma - \hat{\omega}_\gamma$ and $\tilde{\gamma} + \Delta\theta$ are calculated as

$$\frac{d}{dt}\begin{bmatrix} \tilde{\omega}_\gamma \\ \tilde{\gamma} + \Delta\theta \end{bmatrix} = \mathbf{C}\begin{bmatrix} \tilde{\omega}_\gamma \\ \tilde{\gamma} + \Delta\theta \end{bmatrix} \tag{35}$$

where $\mathbf{C} = \begin{bmatrix} 0 & -\rho^2 \\ 1 & -2\rho \end{bmatrix}$.

The characteristic polynomial of $\mathbf{C}$ is represented as

$$\det\left(\mathbf{C} - s\mathbf{I}\right) = s^2 + 2\rho s + \rho^2 \tag{36}$$

The dynamic performance is related to ρ. The selection of ρ is described in part E.

Remark 1: According to (35), in steady state, $\tilde{\gamma}$ converges to $-\Delta\theta$ and $\tilde{\omega}_r$ converges to zero. It is worth mentioning that $\hat{\gamma}$ converges to $\gamma + \Delta\theta$ and $\hat{\omega}_r$ converges to ω_r. It means that a

0278-0046 (c) 2018 IEEE. Personal use is permitted, but republication/redistribution requires IEEE permission. See http://www.ieee.org/publications_standards/publications/rights/index.html for more information.

This article has been accepted for publication in a future issue of this journal, but has not been fully edited. Content may change prior to final publication. Citation information: DOI 10.1109/TIE.2018.2831168, IEEE Transactions on Industrial Electronics

constant angle error $\Delta\theta$ between $\hat{\gamma}$ and γ exists, while no deviation between the estimated rotor speed and the rotor speed.

Remark 2: The stabilization of the sensorless observer is guaranteed if ρ is selected as a positive constant.

D. Upper Bound of the Estimation Error of the Position

Because $|\Delta\theta|=|\Delta\theta_1+\Delta\theta_2|\le|\Delta\theta_1|+|\Delta\theta_2|$, the upper bound of $\Delta\theta_1$ is first taken into consideration, in order to quantitively analyze $\Delta\theta$. It can be seen from Fig. 4, the angle error $|\Delta\theta_1|$ reaches the maximum value $\Delta\theta_{1\max}$ when $O(R_r)$ is orthogonal to $i_c^{\alpha\beta c*}$. The tangent of $\Delta\theta_{1\max}$ could be described as

$$\tan(\Delta\theta_{1\max})=\|O(R_r)\|_2\Big/\left\|i_c^{\alpha\beta c}\right\|_2 \tag{37}$$

Then, according to (27) and (37), the tangent of the angle error $\Delta\theta_{1\max}$ is

$$\tan(\Delta\theta_{1\max})=\left(R_r\left\|i_r^{\alpha\beta r1}\right\|_2\right)\Big/\left(\omega_{slr}L_{hc}\left\|i_c^{\alpha\beta c*}\right\|_2\right) \tag{38}$$

As shown in Appendix I, an upper bound of the tangent of the angle error $\Delta\theta_{1\max}$ is deduced as

$$\tan(\Delta\theta_{1\max})<\left(R_rL_p\left(L_r\omega_{slr}+R_r\right)\right)\Big/\left(\omega_{slr}{}^2L_r\left(L_rL_p-L_{hp}{}^2\right)\right) \tag{39}$$

If $\Delta\theta_{1\max}$ is small, $\tan(\Delta\theta_{1\max})$ can be linearized as $\Delta\theta_{1\max}$, thus the angle $\Delta\theta_{1\max}$ is represented as

$$\Delta\theta_{1\max}<\left(R_rL_p\left(L_r\omega_{slr}+R_r\right)\right)\Big/\left(\omega_{slr}{}^2L_r\left(L_rL_p-L_{hp}{}^2\right)\right) \tag{40}$$

According to (40), $\Delta\theta_{1\max}$ is bounded. Usually, in order to ensure the efficiency of the motor, the ratio between R_r and ω_{slr} is less than 1 % and then $\Delta\theta_{1\max}$ is small. In this paper, $\Delta\theta_{1\max}<0.0616rad$ is achieved by using the BDFIM parameters in Table I.

As shown in Fig. 4, $\Delta\theta_2$ is dependent on $\hat{O}(R_r)$, $\hat{O}(R_r)$ is designed to zero in this paper, which leads to $\Delta\theta_2=0$ and $\Delta\theta=\Delta\theta_1$. Thus, $\tilde{\gamma}$ converges to $-\Delta\theta_1$ based on the analysis in part *C*, the maximum value of $\Delta\theta$ is given as $\Delta\theta_{\max}=\Delta\theta_{1\max}+0=\Delta\theta_{1\max}$.

Remark 3: There exists an optimal $\hat{O}(R_r)$ leading to $\Delta\theta=\Delta\theta_1+\Delta\theta_2=0$, and then $\tilde{\gamma}$ converges to 0. However, such an optimal $\hat{O}(R_r)$ is difficult to obtain in practice. In order to effectively limit the estimated error, designing $\hat{O}(R_r)$ to be zero is reasonable, which leads to a trivial estimated position error as discussed above.

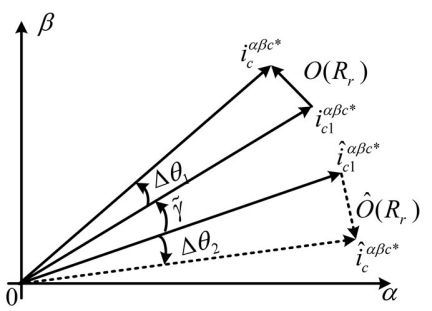

Fig. 4. The relationship between $i_c^{\alpha\beta c*}$, $i_{c1}^{\alpha\beta c*}$, $\hat{i}_{c1}^{\alpha\beta c*}$ and $\hat{i}_c^{\alpha\beta c*}$.

E. Selection of ρ

The poles of the linearized estimator are placed at $s=-\rho$, where ρ is a positive constant, where the selection of ρ is described in [23], which is as follows:

$$\rho=\sqrt{(P_p+P_c)a_s\Delta\omega_r^{ref}\Big/\sin\tilde{\gamma}_{\max}} \tag{41}$$

where $\tilde{\gamma}_{\max}$ is the maximum allowed transient position estimation error, $\Delta\omega_r^{ref}$ represents the speed setpoint and changes in steps, a_s denotes the speed control loop [17] bandwidth in angular frequency.

Remark 4: The dynamic performance is related to ρ according to (35). The maximum allowed transient position estimation error is limited to $\tilde{\gamma}_{\max}$, when selecting ρ based on (41). Then the dynamic performance of the sensorless controller is guaranteed.

F. Global Stability of MRAS observer

In part C of this section, the local stability of the MRAS observer is analyzed based on the assumption that $\tilde{\gamma}+\Delta\theta$ is small. However, this analysis is invalid when $\tilde{\gamma}+\Delta\theta$ is large, especially when the algorithm kicks in. In this part, the global stability of the proposed MRAS observer is analyzed by means of LaSalle's invariance principle.

According to (18), (19), (28), (30), (33) and (34), the estimation error $\tilde{\omega}_\gamma$ and $\tilde{\gamma}+\Delta\theta$ are calculated as

$$d\left[\tilde{\omega}_\gamma\quad\tilde{\gamma}+\Delta\theta\right]^T\Big/dt=\mathbf{C}\left[\tilde{\omega}_\gamma\quad\sin(\tilde{\gamma}+\Delta\theta)\right]^T \tag{42}$$

A Lyapunov function candidate is designed as

$$V\left(\tilde{\omega}_\gamma,\tilde{\gamma}+\Delta\theta\right)=\tilde{\omega}_\gamma^2\Big/2+\rho^2(1-\cos(\tilde{\gamma}+\Delta\theta)) \tag{43}$$

and $\dot{V}=-2\rho^3\sin^2(\tilde{\gamma}+\Delta\theta)$. If $\rho>0$, $\dot{V}\le0$. Let E be the set of all point where $\dot{V}=0$ and it is described as

$$E=\{\tilde{\gamma}+\Delta\theta\in R\,|\,\tilde{\gamma}+\Delta\theta=2n\pi\} \tag{44}$$

where n is an integer and R is the set of all real numbers. According to (42), $\tilde{\omega}_\gamma=0$, if $\tilde{\gamma}+\Delta\theta=2n\pi$. Thus, E could be described as

$$E=\{\tilde{\gamma}+\Delta\theta\in R,\tilde{\omega}_\gamma\in R\,|\,\tilde{\gamma}+\Delta\theta=2n\pi,\tilde{\omega}_\gamma=0\} \tag{45}$$

Meanwhile, $V=0$ if $\{\tilde{\gamma}+\Delta\theta,\tilde{\omega}_\gamma\}\in E$ and $V>0$ if $\{\tilde{\gamma}+\Delta\theta,\tilde{\omega}_\gamma\}\notin E$. $\dot{V}<0$ if $\{\tilde{\gamma}+\Delta\theta,\tilde{\omega}_\gamma\}\notin E$. Thus, $\{\tilde{\gamma}+\Delta\theta,\tilde{\omega}_\gamma\}\in E$ are asymptotically stable points.

It could be concluded that E will be the largest invariant set itself and every point start from anywhere will approach E as $t\to\infty$. $\{\tilde{\gamma}+\Delta\theta,\tilde{\omega}_\gamma\}\in E$ are globally asymptotically stable points.

G. Parameter Sensitivity Analysis

Since (16) is constructed based on the assumption that the motor parameters are perfectly correct, which is untenable for practical applications. Then, (16) is revised as follows:

0278-0046 (c) 2018 IEEE. Personal use is permitted, but republication/redistribution requires IEEE permission. See http://www.ieee.org/publications_standards/publications/rights/index.html for more information.

This article has been accepted for publication in a future issue of this journal, but has not been fully edited. Content may change prior to final publication. Citation information: DOI 10.1109/TIE.2018.2831168, IEEE Transactions on Industrial Electronics

$$\hat{i}_{c1}^{\alpha\beta c*} = e^{-j\tilde{\gamma}}\left(\hat{L}_{hp}^{\ 2} - \hat{L}_r\hat{L}_p\right)\left(\hat{\sigma}\psi_p^{\alpha\beta p} + i_p^{\alpha\beta p}\right)\Big/\left(\hat{L}_{hp}\hat{L}_{hc}\right) \quad (46)$$

where $\hat{\sigma} = \hat{L}_r\Big/\left(\hat{L}_{hp}^{\ 2} - \hat{L}_r\hat{L}_p\right)$

Meanwhile, (17) is revised as follows:

$$\varepsilon = \mathrm{Im}(\hat{i}_{c1}^{\alpha\beta c*} i_c^{\alpha\beta c}) \quad (47)$$

According to (16) and (46), the relationship between $\hat{i}_{c1}^{\alpha\beta c*}$ and $\hat{i}_c^{\alpha\beta c*}$ is described as follows:

$$\hat{i}_c^{\alpha\beta c*} = \left(\left\|\hat{i}_c^{\alpha\beta c*}\right\|_2 \hat{i}_{c1}^{\alpha\beta c*} e^{-j\Delta\zeta}\right)\Big/\left\|\hat{i}_{c1}^{\alpha\beta c*}\right\|_2 \quad (48)$$

The angle between these two vectors $\Delta\zeta$ is derived in Appendix II.

According to (21), (22) and (47), the relationship between $\hat{i}_{c1}^{\alpha\beta c*}$ and $i_c^{\alpha\beta c}$ is described as

$$i_c^{\alpha\beta c*} = \left(\left\|i_c^{\alpha\beta c*}\right\|_2 \hat{i}_{c1}^{\alpha\beta c*} e^{-j(\Delta\zeta+\Delta\theta+\tilde{\gamma})}\right)\Big/\left\|\hat{i}_{c1}^{\alpha\beta c*}\right\|_2 \quad (49)$$

Thus, (30) is revised as

$$\varepsilon = \left\|i_c^{\alpha\beta c*}\right\|_2 \left\|\hat{i}_{c1}^{\alpha\beta c*}\right\|_2 \sin(\tilde{\gamma} + \Delta\theta + \Delta\zeta) \quad (50)$$

Remark 5: Based on the global stability analysis in part *F* of this section, the estimated position error $\tilde{\gamma}$ converges to $-\Delta\theta - \Delta\zeta$ and the estimated speed error converges to zero. The mismatch parameters lead to a constant error $\Delta\zeta$ of $\tilde{\gamma}$. Meanwhile, $\tilde{\omega}_\gamma$=0 is still the asymptotically points. Thus, the mismatches parameters have no influence on the estimated speed.

IV. Experimental Results

A. Experimental Setup and Implementation

In order to evaluate the proposed algorithm, sets of experimental results are generated by executing the comprehensive sensorless control scheme presented in Fig. 3, based on a 30 kW BDFIM with wound-type rotor [5] platform given in Fig. 5, while the machine specification and parameters are tabulated in Table I, it is worth noting that the parameters are transformed to the PW side.

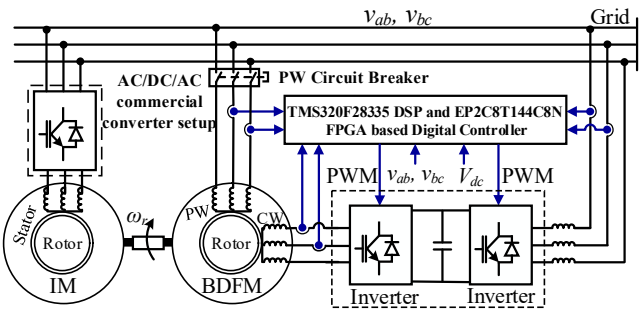

Fig. 5. Schematic block diagram of the BDFIM experimental setup.

TABLE I

THE BDFIM PARAMETERS AND RATINGS

Parameter	Value	Parameter	Value
L_{hp}	0.4663 H	R_c	0.44304 Ω
L_{hc}	0.0488 H	J	0.95 kgm²
L_p	0.4706 H	PW rated voltage	380 V/50 Hz
L_c	0.0510 H	PW rated power	30 kW
L_r	0.5233 H	Natural speed	78.5 rad/s
R_r	0.78524 Ω	PW poles	2
R_p	0.40355 Ω	CW poles	6

The PW of the BDFIM is grid-connected via (380 V/50 Hz), and CW of the BDFIM is driven by a PWM inverter with a switching frequency of 4 kHz, and the sampling angular frequency ω_{samp} of the control loop is 8000π rad/s. The CW current control algorithm was implemented on a digital signal processor (DSP, TMS32028335) and a field-programmable gate array (FPGA, EP2C8J144C8N), where the DSP is mainly in charge of the CW current control algorithm implementation. While the FPGA takes charge of generating the driving signals for insulated gate bipolar transistor (IGBT). The PW and CW currents are measured with VSM025A and CHB500-SG respectively. Speed and position signals are obtained from an incremental encoder, E6B2-CWZ6C, with a resolution of 2000 cycles/r, provided by OMRON. A 30 kW eight-pole induction machine is mechanically coupled to the 30 kW BDFIM to provide the required speed. The induction machine is equipped with a commercial ac drive (INVT, GOODRIVE35). The inverter uses a 650V dc-link-voltage. Both the dc-link-voltage and ac drive are supplied by a commercial rectifier (INVT, GOODRIVE800). The schematic block diagram of the experimental setup and the test rig of the BDFIM experimental setup are shown in Fig. 6, respectively.

B. Start-up procedure of the BDFIM

The first step of the start-up is to establish the *d*-axis CW current so that the induced PW voltage equals to the grid voltage and then the sensorless control works. The *d*-axis CW current reference is obtained based on the error between the amplitude of induced PW voltage and grid voltage, while a common PI regulator is used to eliminate the error. Simultaneously, the proposed observer kicks in. When the induced PW voltage successfully follows the grid voltage, the PW circuit breaker is closed as shown in Fig. 5. Then, the speed reference is set up and start-up of the BDFIM is carried out.

Figure 7 shows the experimental results of the initial transients of the BDFIM considering the aforementioned procedure. The initial transients before and after the PW circuit breaker is closed are shown in Fig. 7(a) and (b), respectively. In Fig. 7(a), the line-to-line grid voltage u_{AB}^{grid}, the line-to-line PW voltage u_{AB}^{PW} and the CW current i_A^{CW} are shown. From Fig. 7(a), the *d*-axis CW current is established first consequently the induced PW voltage successfully tracks the grid voltage, which means the MRAS observer has converged. In Fig. 7(b), the speed reference, speed, estimated position and speed error are expressed in red, blue, green and magenta, respectively. Note that the same signal color coordination and units apply for rest of the following figures, thus no need to repeat throughout. From Fig. 7(b), the speed reference was set up at 2.2s and the start-up of the BDFIM has been successfully engaged and operational.

0278-0046 (c) 2018 IEEE. Personal use is permitted, but republication/redistribution requires IEEE permission. See http://www.ieee.org/publications_standards/publications/rights/index.html for more information.

This article has been accepted for publication in a future issue of this journal, but has not been fully edited. Content may change prior to final publication. Citation information: DOI 10.1109/TIE.2018.2831168, IEEE Transactions on Industrial Electronics

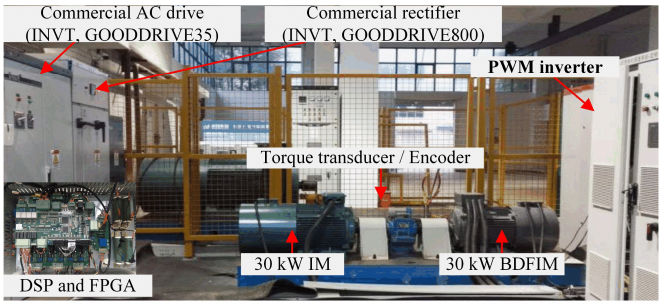

Fig. 6. The test rig of the BDFIM experimental setup.

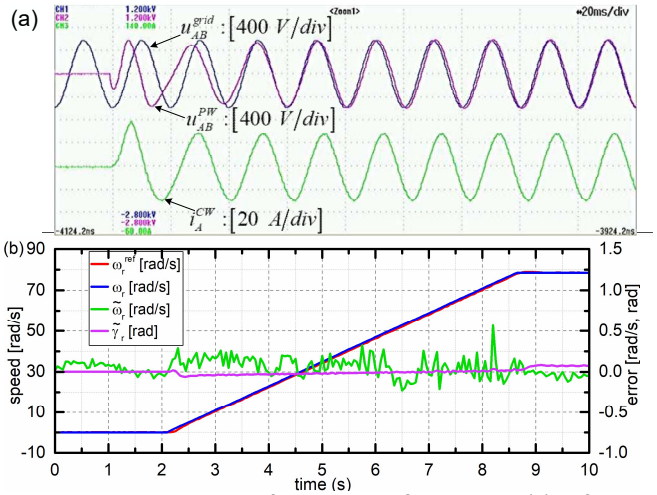

Fig. 7. Experimental results of the start-up of the BDFIM. (a) Before the PW circuit breaker is closed (b) After the PW circuit breaker is closed.

C. Dynamic Responses

Usually, the BDFIM does not work at the low speeds in practical wind generator application because its partial-power feature, thus the dynamic performance at low speeds is not discussed in this paper. Considering the trade-off between the cost of the PWM converter and the speed range, typically, the converter rating is generally about one-third of the rating of the generator, and the BDFIM works from 67% rated speed to 133% rated speed in this case. The maximum value of ω_{slr} is equal to 33.33π rad/s, thus, the minimum value of ω_r is equal to 66.67π rad/s. $\Delta\theta_{max}$ is calculated less than 0.0616 rad, which lead to trivial estimated position error on the proposed MRAS observer in steady state.

To evaluate the estimating performance, γ and ω_r are obtained from the incremental encoder, and $\hat{\gamma}$ and $\hat{\omega}_r$ are estimated from the MRAS observer. Figs. 8 and 9 show the captured experimental results for the estimated position and speed error when the speed changing at no-load and full-load in a ramp fashion respectively. The speed reference is given as a ramp signal. The experimental results show that the estimated position and speed error is trivial when speed changing at different operation modes.

Figures 10 and 11 illustrate the experimental results for the estimated position and speed error in response to a sudden decrease and/or sudden increase in load. The loading condition

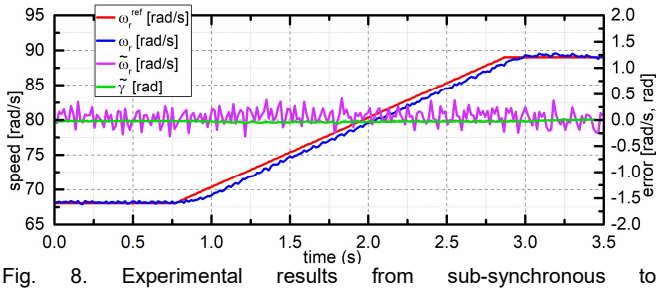

Fig. 8. Experimental results from sub-synchronous to super-synchronous mode at no-load.

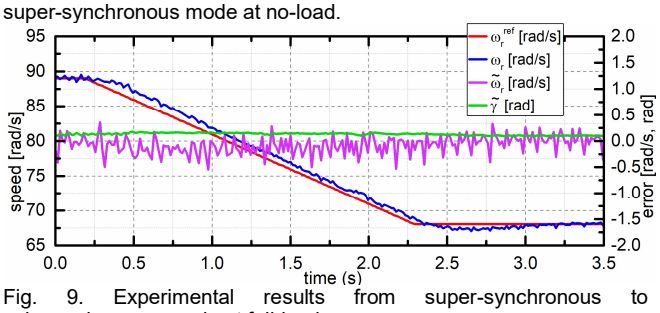

Fig. 9. Experimental results from super-synchronous to sub-synchronous mode at full-load.

is controlled by changing the electromagnetic torque reference of the 30kW eight-pole IM in a form of a step signal, based around sub-synchronous, synchronous and super-synchronous speed operations. The speed decreases when the load increases indicating that the estimated position and speed error is small when workload condition changing suddenly. The speed control loop bandwidth a_s and the maximum allowed transient position estimation error $\tilde{\gamma}_{max}$ are designed to be equal to 5π rad/s and 0.174 rad. From the experimental results, the error between the estimated position and the position of the CW is about ±0.25 rad, and the error between the estimated rotor speed and the rotor speed is about ±0.5 rad/s.

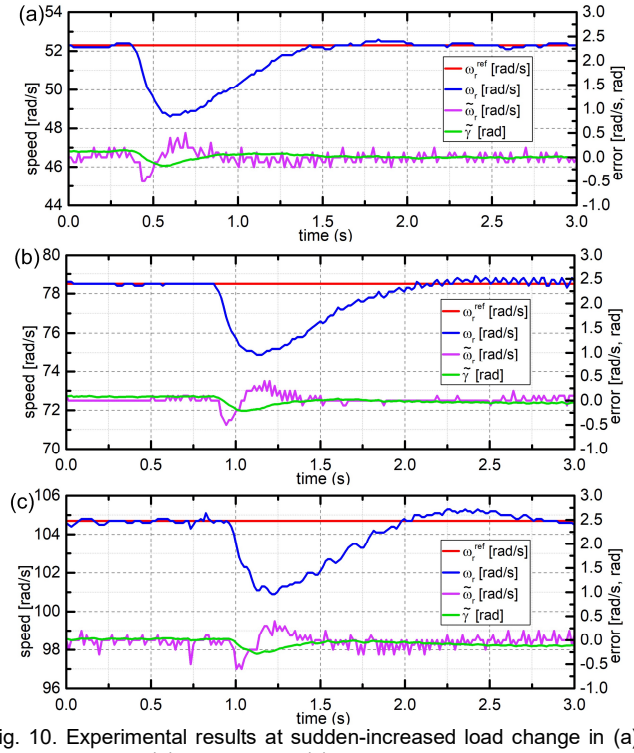

Fig. 10. Experimental results at sudden-increased load change in (a) sub-synchronous (b) synchronous (c) super-synchronous modes.

0278-0046 (c) 2018 IEEE. Personal use is permitted, but republication/redistribution requires IEEE permission. See http://www.ieee.org/publications_standards/publications/rights/index.html for more information.

This article has been accepted for publication in a future issue of this journal, but has not been fully edited. Content may change prior to final publication. Citation information: DOI 10.1109/TIE.2018.2831168, IEEE Transactions on Industrial Electronics

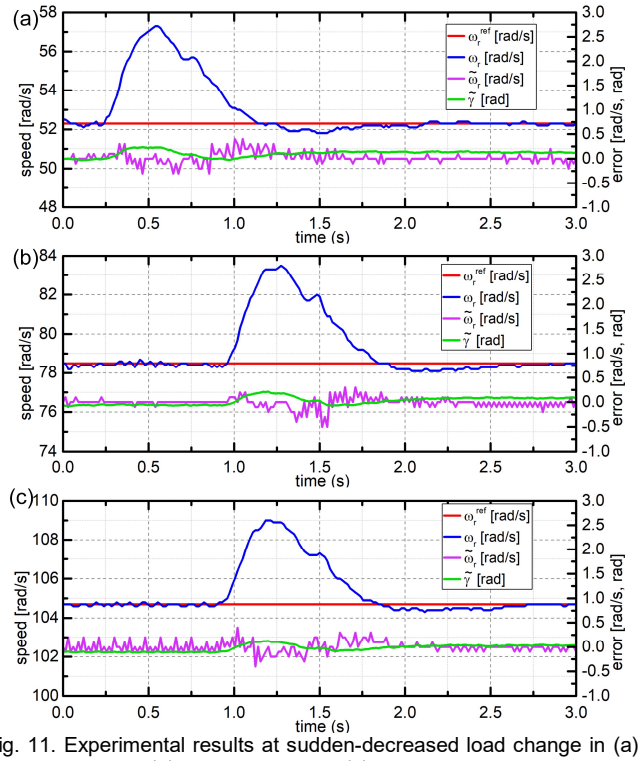

Fig. 11. Experimental results at sudden-decreased load change in (a) sub-synchronous (b) synchronous and (c) super-synchronous modes.

Fig. 12 shows the experimental results of the estimated positions and speed errors when the speed reference decreases in steps from 88.97 rad/s (850 rpm) to 83.73 rad/s (800 rpm) and increases from 83.73 rad/s (800 rpm) to 88.97 rad/s (850 rpm), where both no-load and full-load operating conditions are considered. The speed control loop bandwidth α_s and the maximum allowed transient position estimation error $\tilde{\gamma}_{\max}$ are designed to be 5π rad/s and 0.08 rad respectively. From the experimental results, the error between the estimated position and the actual position is about ±0.25 rad, and the error between the estimated rotor speed and the rotor speed is about ±0.5 rad/s. Thus, results indicate that the estimated errors (position and speed) are small when speed reference suddenly changes at different loading profiles. The derivative of rotor speed is not zero, due to the system disturbance, the speed control performance and so on. However, the speed error is still trivial in terms of the amplitude of the rotor speed, the amplitude of the speed error is within 0.7 rad/s in the steady and dynamic state, and the relative error is less than 0.89% of the speed. In this case, the error is relatively "trivial", and its impact on speed control is neglected.

D. Parameter Sensitivity

In this paper, the rated PW voltage is 380 V/50 Hz. Thus, $\left\|\psi_p^{\alpha\beta p}\right\|_2$ is about 1 Wb, meanwhile, $\left\|i_p^{\alpha\beta p}\right\|_2$ is depended on the load according to Table I, $\sigma = -18.1517$. Here the ratio of the estimated $\hat{\sigma}$ and σ is defined as k_σ. Moreover, Fig. 13 shows experimental results of estimated speed error $\tilde{\omega}_r$ with different $\left\|i_p^{\alpha\beta p}\right\|_2$ and $\hat{\sigma}$ indicating that error estimating of σ has no impact on $\tilde{\omega}_r$.

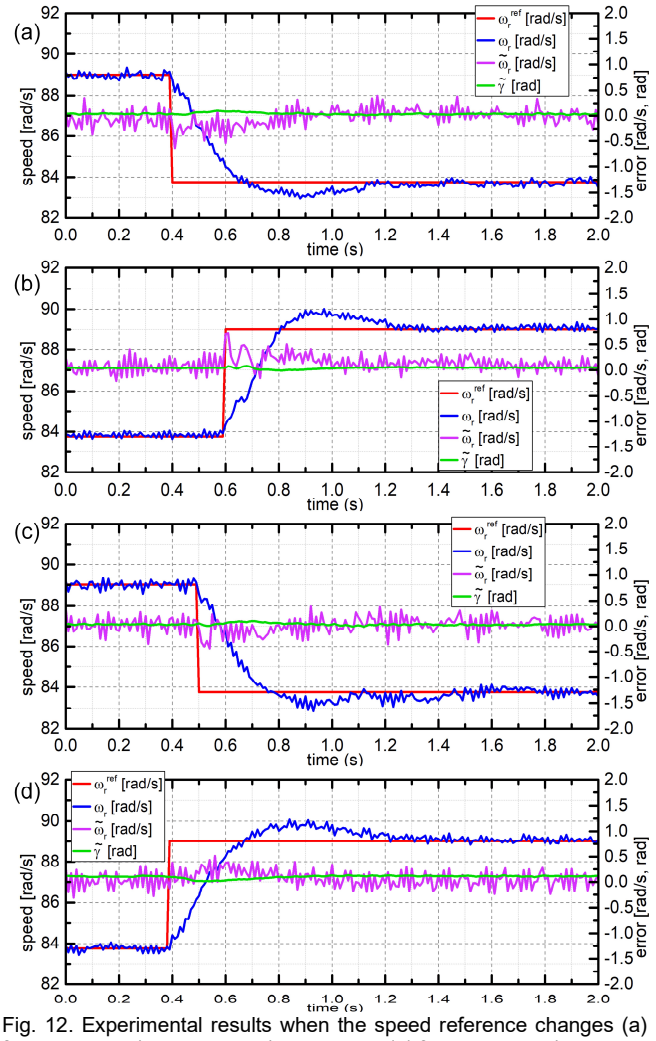

Fig. 12. Experimental results when the speed reference changes (a) from 88.97 rad/s to 83.73 rad/s at no-load, (b) from 83.73 rad/s to 88.97 rad/s at no-load, (c) from 88.97 rad/s to 83.73 rad/s at full-load, and (d) from 83.73 rad/s to 88.97 rad/s at full-load.

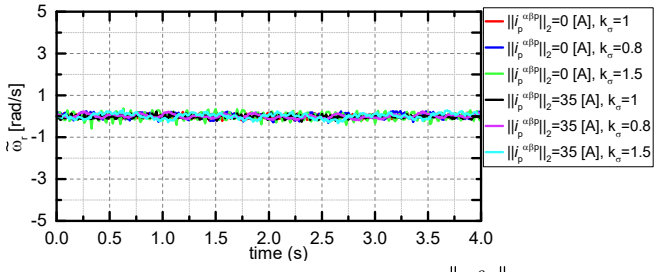

Fig. 13. Estimated speed error $\tilde{\omega}_r$ with different $\left\|i_p^{\alpha\beta p}\right\|_2$ and k_σ.

Evidently, Fig. 14 shows the relationship between $\left\|i_p^{\alpha\beta p}\right\|_2$, $\hat{\sigma}$ and $\Delta\zeta$ based on (54) in Appendix II, exhibiting that overestimating σ leads to positive $\Delta\zeta$, while underestimating σ leads to negative $\Delta\zeta$. Fig. 15 shows experimental results of estimated position error $\tilde{\gamma}$ with different $\left\|i_p^{\alpha\beta p}\right\|_2$ and $\hat{\sigma}$, reveals that error estimation of σ leads to a constant error of $\tilde{\gamma}$. Furthermore, overestimating σ exactly leads to positive $\Delta\zeta$, while underestimating σ will exactly lead negative $\Delta\zeta$,

0278-0046 (c) 2018 IEEE. Personal use is permitted, but republication/redistribution requires IEEE permission. See http://www.ieee.org/publications_standards/publications/rights/index.html for more information.

This article has been accepted for publication in a future issue of this journal, but has not been fully edited. Content may change prior to final publication. Citation information: DOI 10.1109/TIE.2018.2831168, IEEE Transactions on Industrial Electronics

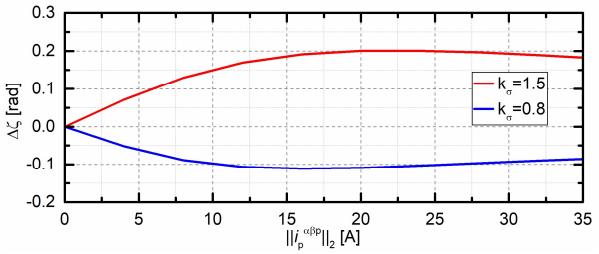

Fig. 14. The relationship between $\left\|i_p^{\alpha\beta p}\right\|_2$, $\Delta\zeta$ and k_σ.

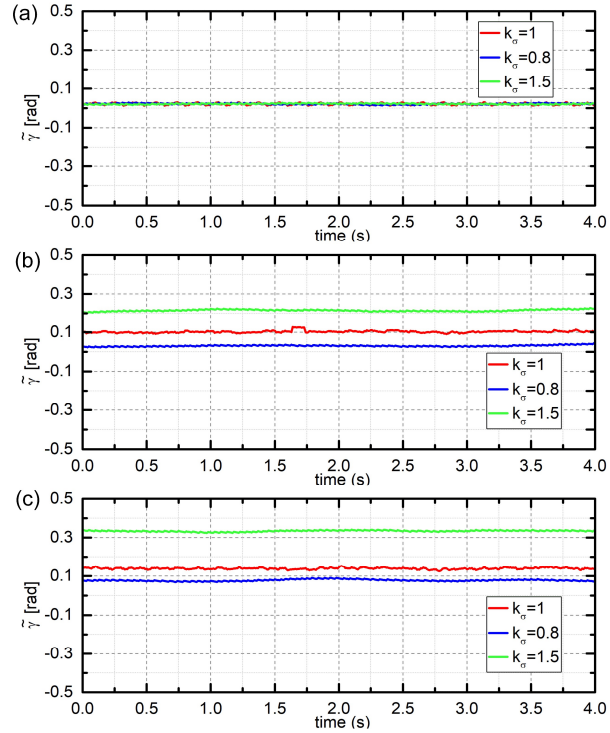

Fig. 15. Experimental results for estimated position error $\tilde{\gamma}$ at with different $\left\|i_p^{\alpha\beta p}\right\|_2$ and k_σ : (a) 0 A, (b) 14 A, and (c) 28 A.

which is consistent with the theoretical analysis in (54) in Appendix II.

V. Conclusion

In this paper, an original control winding current-based MRAS observer is designed and experimentally validated for the sensorless control of the adjustable speed BDFIM, and an estimator similar to a PLL is used to estimate the CW position and rotor speed. The proposed method has shown good steady-state and dynamic performance. There is no steady state error in the rotor speed estimation, while a trivial angle error is caused by the estimated position and position of the CW. The effectiveness, robustness (to uncertainties toward parameter variations), correctness, and feasibility of the proposed method have been demonstrated and verified for the challenging speed dependent loading circumstances.

Appendix I

Since it is assumed that the current converges to a steady-state solution, according to (11) and (12), the relationship between the PW current, CW current and rotor current in the general synchronously rotating *d*-*q* reference frame is given by

$$0 = R_r i_r^{dq} + j\omega_{slr}\left(L_r i_r^{dq} + L_{hp} i_p^{dq} + L_{hc} i_c^{dq}\right) \quad (51)$$

Assuming that the stator flux-oriented vector control strategy is adopted, then $\psi_p^q = 0$. According to (8), the *q*-axis PW current can be derived as $i_p^q = -L_{hp} i_r^q / L_p$. Usually, the *d*-axis PW current is controlled to zero, then $i_p^d = 0$. According to (51), i_r^{dq} is described as $\mathbf{A}\left[i_r^d \quad i_r^q\right]^T = -\left[i_c^d \quad i_c^q\right]^T$, where

$$\mathbf{A} = \begin{bmatrix} L_r/L_{hc} & R_r/\left(L_{hc}\omega_{slr}\right) \\ -R_r/\left(L_{hc}\omega_{slr}\right) & L_r/L_{hc} - L_{hp}L_{hp}/\left(L_{hc}L_p\right) \end{bmatrix}$$

The relationship can also be represented as

$$\left[i_r^d \quad i_r^q\right]^T = -\mathbf{B}\left[i_c^d \quad i_c^q\right]^T \quad (52)$$

where $\mathbf{B} = \mathbf{A}^{-1}$. According to the triangle inequality [24], an upper bound of l_2-norm of i_r^{dq} is described as

$$\left\|\begin{bmatrix} i_r^d \\ i_r^q \end{bmatrix}\right\| = \left\|\begin{bmatrix} \mathbf{B}(1,1) & \mathbf{B}(1,2) \\ \mathbf{B}(2,1) & \mathbf{B}(2,2) \end{bmatrix}\begin{bmatrix} i_c^d \\ i_c^q \end{bmatrix}\right\|_2 \le \left(\left\|\begin{bmatrix} \mathbf{B}(1,1) & 0 \\ 0 & \mathbf{B}(2,2) \end{bmatrix}\right\|_2 + \left\|\begin{bmatrix} 0 & \mathbf{B}(1,2) \\ \mathbf{B}(2,1) & 0 \end{bmatrix}\right\|_2\right)\left\|\begin{bmatrix} i_c^d \\ i_c^q \end{bmatrix}\right\|_2$$

Since rotation transformation will not change l_2-norm of a vector, then

$$\left(\left\|i_r^{\alpha\beta r1}\right\|_2 \Big/ \left\|i_c^{\alpha\beta c*}\right\|_2\right) \le \left(\left\|\begin{bmatrix} \mathbf{B}(1,1) & 0 \\ 0 & \mathbf{B}(2,2) \end{bmatrix}\right\|_2 + \left\|\begin{bmatrix} 0 & \mathbf{B}(1,2) \\ \mathbf{B}(2,1) & 0 \end{bmatrix}\right\|_2\right) \quad (53)$$

According to (38) and (53), the upper bound of the tangent of the angle error $\Delta\theta_{1\max}$ is

$$\tan\left(\Delta\theta_{1\max}\right) \le \frac{R_r}{\omega_{slr}L_{hc}}\left\|\begin{bmatrix} \mathbf{B}(1,1) & 0 \\ 0 & \mathbf{B}(2,2) \end{bmatrix}\right\|_2 + \left\|\begin{bmatrix} 0 & \mathbf{B}(1,2) \\ \mathbf{B}(2,1) & 0 \end{bmatrix}\right\|_2$$

$$< \frac{R_r\left(\mathbf{A}(1,1) + \mathbf{A}(1,2)\right)}{\omega_{slr}L_{hc}\mathbf{A}(1,1)\mathbf{A}(2,2)} = \frac{R_r L_p\left(L_r\omega_{slr} + R_r\right)}{\omega_{slr}^2 L_r\left(L_r L_p - L_{hp}^2\right)}$$

Appendix II

Since the angle between two vectors is independent on their amplitudes. For simplicity, the angle $\Delta\zeta$ between $\hat{i}_{c1}^{\alpha\beta c*}$ and $\hat{i}_c^{\alpha\beta c*}$ is calculated as the angle between $v_1 = e^{-j\hat{\gamma}}\left(\sigma\psi_p^{\alpha\beta p} + i_p^{\alpha\beta p}\right)$ and $v_2 = e^{-j\hat{\gamma}}\left(\hat{\sigma}\psi_p^{\alpha\beta p} + i_p^{\alpha\beta p}\right)$ as $\hat{O}(R_r)$ is designed to zero, where $\sigma = L_r/\left(L_{hp}^2 - L_r L_p\right)$. The parametric sensitivity of the proposed sensorless controller is summed up to the parameter sensitivity of σ.

Usually, the PW flux field-oriented vector control is used and the reactive power of PW side is controlled to zero. Thus, $\psi_p^{\alpha\beta p}$ is orthogonal to $i_p^{\alpha\beta p}$. Fig. 16 shows the relationship between the two vectors v_1 and v_2. Based on Trigonometric formulas, $\Delta\zeta$ is described as

$$\Delta\zeta = \arcsin\left(\left(\tan\theta_2 - \tan\theta_1\right)\cos\theta_1\cos\theta_2\right) \quad (54)$$

0278-0046 (c) 2018 IEEE. Personal use is permitted, but republication/redistribution requires IEEE permission. See http://www.ieee.org/publications_standards/publications/rights/index.html for more information.

This article has been accepted for publication in a future issue of this journal, but has not been fully edited. Content may change prior to final publication. Citation information: DOI 10.1109/TIE.2018.2831168, IEEE Transactions on Industrial Electronics

where $\tan\theta_1 = \left\|i_p^{\alpha\beta p}\right\|_2 / \left\|\sigma\psi_p^{\alpha\beta p}\right\|_2$, $\tan\theta_2 = \left\|i_p^{\alpha\beta p}\right\|_2 / \left\|\hat{\sigma}\psi_p^{\alpha\beta p}\right\|_2$

and $\cos\theta_1\cos\theta_2 = \left\|\sigma\psi_p^{\alpha\beta p}\right\|_2 \left\|\hat{\sigma}\psi_p^{\alpha\beta p}\right\|_2 \Big/ \left\|\sigma\psi_p^{\alpha\beta p} + i_p^{\alpha\beta p}\right\|_2 \left\|\hat{\sigma}\psi_p^{\alpha\beta p} + i_p^{\alpha\beta p}\right\|_2$

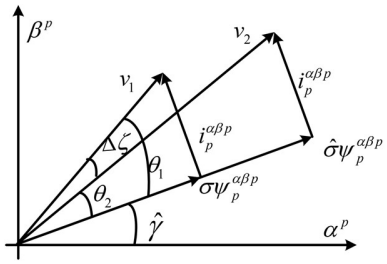

Fig. 16. The relationship between v_1 and v_2 .

REFERENCES

[1] R. Saidur, S. Mekhief, M. B. Ali, A. Safari and H. A. Mohammed, "Applications of variable speed drive (VSD) in electrical motors energy savings," *Renew. Sust. Energ. Rev.*, Vol. 16, pp. 543-550, Jan. 2012.

[2] M. Cheng and Y. Zhu, "The state of the art of wind energy conversion system and technologies: a review," *Energ. Convers. Manage.*, Vol. 88, pp. 332-347, Dec. 2014.

[3] T. D. Strous, H. Polinder and J. A. Ferreira, "Brushless doubly-fed induction machines for wind turbines: developments and research challenges," *IET Electr. Power Appl.*, Vol. 11, pp. 991-1000, July 2016.

[4] R. A. McMahon, X. Wan , E. Abdi-Jalebi, P. J. Tavner, P. C. Roberts, M. Jagiela, "The BDFM as a generator in wind turbines," *Proc. 12th Int. Power Electron. Motion Control Conf.*, pp. 1859–1869, Aug. 2006.

[5] F. Xiong and X. Wang, "Design of a low-harmonic-content wound rotor for the brushless doubly fed generator," *IEEE Trans. on Energy Convers.*, Vol. 29, pp. 158–168, Mar. 2014.

[6] P. C. Roberts. "A study of brushless doubly-fed (induction) machines," *Ph.D. dissertation*, Emanuel College, University of Cambridge., England, 2004.

[7] S. Ademi and M. G. Jovanovic, "Control of emerging brushless doubly-fed reluctance wind turbine generators," *in Large Scale Renewable Power Generation* (*Ser. Green Energy and Technology*), Eds. Berlin, Germany: Springer-Verlag, pp. 395-411, 2014.

[8] S. Ademi and M. Jovanović, "A novel sensorless speed controller design for doubly-fed reluctance wind turbine generators," *Energ. Convers. Manage.*, Vol. 120, pp. 229-237, Jul. 2016.

[9] R. Cardenas, R. Pena, J. Proboste, G. Asher and J. Clare, "MRAS observer for sensorless control of standalone doubly fed induction generators," *IEEE Trans. on Energy Convers.,* Vol. 20, pp. 710-718, Dec. 2005.

[10] R. Pena, R. Cardenas, J. Proboste, G. Asher and J. Clare, "Sensorless control of doubly-fed induction generators using a rotor-current-based MRAS observer," *IEEE Trans. on Ind. Electron.*, Vol. 55, pp. 330-339, Jan. 2008.

[11] R. Cardenas, R. Pena, J. Clare, G. Asher and J. Proboste, "MRAS observers for sensorless control of doubly-fed induction generators," *IEEE Trans. on Power Electron.*, Vol. 23, pp. 1075-1084, May. 2008.

[12] M. S. Carmeli, F. C. Dezza, M. Iacchetti and R. Perini, "Effects of mismatched parameters in MRAS sensorless doubly fed induction machine drives," *IEEE Trans. on Power Electron.*, Vol. 25, pp. 2842-2851, Nov. 2010.

[13] M. F. Iacchetti, "Adaptive tuning of the stator inductance in a rotor-current-based MRAS observer for sensorless doubly fed induction-machine drives," *IEEE Trans. on Ind. Electron.*, Vol. 58, pp. 4683-4692, Oct. 2011.

[14] M. Jovanovic, "Sensored and sensorless speed control methods for brushless doubly fed reluctance motors," *IET Electr. Power Appl.*, Vol. 3, pp. 503-513, Nov. 2009.

[15] S. Ademi, M. G. Jovanović, H. Chaal and W. Cao, "A new sensorless speed control scheme for doubly fed reluctance generators," *IEEE Trans. on Energy Convers.*, Vol. 31, pp. 993-1001, Sept. 2016.

[16] S. Tohidi, "Analysis and simplified modelling of brushless doubly-fed induction machine in synchronous mode of operation," *IET Electr. Power Appl.*, Vol 10, pp. 110-116, Feb 2016.

[17] G. Zhang, J. Yang, M. Su, W. Tang, and F. Blaabjerg, "Stator-current-based MRAS observer for the sensorless control of the brushless doubly-fed induction machine," *IEEE Applied Power Electronics Conference and Exposition*, pp. 3150-3155, Mar. 2017.

[18] N. Patin, E. Monmasson and J. Louis, "Modeling and control of a cascaded doubly fed induction generator dedicated to isolated grids," *IEEE Trans. on Ind. Electron.*, Vol. 56, pp. 4207-4219, Oct. 2009.

[19] G. Esfandiari, M. Ebrahimi, A. Tabesh and M. Esmaeilzadeh, "Dynamic modeling and analysis of cascaded DFIMs in an arbitrary reference frame," *IEEE Trans. on Energy Convers.*, Vol. 30, pp. 999-1007, Sept. 2015.

[20] J. Poza, E. Oyarbide, D. Roye and M. Rodriguez, "Unified reference frame dq model of the brushless doubly fed machine," *Proc. Inst. Elect. Eng. Elect. Power Appl.*, Vol. 153, pp. 726-734, Sept. 2006.

[21] G. Zhang, J. Yang, Y. Sun, M. Su, W. Tang, Q. Zhu and H. Wang, "A robust control scheme based on ISMC for the brushless doubly fed induction machine", *IEEE Trans. on Power Electron.*, Vol. 33, pp. 3129-3140, Apr. 2018.

[22] J. Holtz, "Sensorless control of induction motor drives," *Proceedings of the IEEE*, Vol. 90, pp. 1359-1394, Aug. 2002.

[23] L. Harnefors and H. P. Nee, "A general algorithm for speed and position estimation of AC motors," *IEEE Trans. on Ind. Electron.*, pp. 77-83, Feb. 2000.

[24] R. A. Horn and C. R. Johnson. *Matrix analysis*. 2n ed., Utah, USA, Cambridge University press, 2013, pp. 340-341.

Jian Yang (M' 09) received the Ph.D. degree in electrical engineering from the University of Central Florida, Orlando, in 2008. He was a Senior Electrical Engineer been with Delta Tau Data Systems, Inc., Los Angeles, CA, from 2007 to 2010. Since 2011, he has been with Central South University, Changsha, China, where he is currently a Professor with the School of Information Science and Engineering.

His main research interests include motion control, power electronics and its applications in wind energy generation system and photovoltaic system.

Weiyi Tang was born in Jiangsu, China, in 1991. He received his B.S. degree in Automation from Central South University, Changsha, China, in 2013, where he is now pursuing Ph.D. degree in Control Science and Engineering.

His research interests include motion control and wireless power transfer.

Guanguan Zhang received the B.S. degree from Central South University, Changsha, China, in 2012, where she is working toward the Ph.D. degree in power electronics and power transmission. She was a joint Ph.D. student supported by the China Scholarship Council with the Department of Energy Technology, Aalborg University, Aalborg, Denmark, where she focuses on the reliability analysis of wind power system.

Her research interests include matrix converter, motor control and wind power system.

Yao Sun (M'13) was born in Hunan, china, in 1981. He received the B.S., M.S. and Ph.D. degrees from the School of Information Science and Engineering, Central South University, Changsha, China, in 2004, 2007 and 2010, respectively. He has been an associate professor with the School of Information Science and Engineering, Central South University, China.

His research interests include matrix converter, micro-grid and wind energy conversion system.

0278-0046 (c) 2018 IEEE. Personal use is permitted, but republication/redistribution requires IEEE permission. See http://www.ieee.org/publications_standards/publications/rights/index.html for more information.

This article has been accepted for publication in a future issue of this journal, but has not been fully edited. Content may change prior to final publication. Citation information: DOI 10.1109/TIE.2018.2831168, IEEE Transactions on Industrial Electronics

Sul Ademi (M'12) received the B.Eng. and Ph.D. degrees in Electrical and Electronics Engineering from Northumbria University at Newcastle upon Tyne, U.K., in 2011 and 2014, respectively. From 2015 to 2017, he was a Lead Researcher engaged in knowledge exchange and transfer partnership activities between University of Strathclyde, Glasgow, U.K and GE Grid Solutions, Stafford, U.K., where he focused on the development of novel DC protection schemes suitable for protecting future high-voltage direct current (HVDC) transmission systems. He is currently a Research Scientist with the Warwick Manufacturing Group, University of Warwick, Coventry, U.K. His main interests are in the areas of electric motor drives, validation of high-performance controllers for variable-speed applications, applications and control of doubly-fed machines, and design and analysis of novel permanent-magnet machines.

Frede Blaabjerg (S'86–M'88–SM'97–F'03) was with ABB-Scandia, Randers, Denmark, from 1987 to 1988. From 1988 to 1992, he got the PhD degree in Electrical Engineering at Aalborg University in 1995. He became an Assistant Professor in 1992, an Associate Professor in 1996, and a Full Professor of power electronics and drives in 1998. From 2017 he became a Villum Investigator.

His current research interests include power electronics and its applications such as in wind turbines, PV systems, reliability, harmonics and adjustable speed drives. He has published more than 500 journal papers in the fields of power electronics and its applications. He is the co-author of two monographs and editor of 7 books in power electronics and its applications.

He has received 24 IEEE Prize Paper Awards, the IEEE PELS Distinguished Service Award in 2009, the EPE-PEMC Council Award in 2010, the IEEE William E. Newell Power Electronics Award 2014 and the Villum Kann Rasmussen Research Award 2014. He was the Editor-in-Chief of the IEEE TRANSACTIONS ON POWER ELECTRONICS from 2006 to 2012. He has been Distinguished Lecturer for the IEEE Power Electronics Society from 2005 to 2007 and for the IEEE Industry Applications Society from 2010 to 2011 as well as 2017 to 2018. In 2018 he is President Elect of IEEE Power Electronics Society.

He is nominated in 2014, 2015, 2016 and 2017 by Thomson Reuters to be between the most 250 cited researchers in Engineering in the world. In 2017 he became Honoris Causa at University Politehnica Timisoara (UPT), Romania.

Qi Zhu was born in Anhui Province, China, in 1993. He received the B.S. degree in electrical engineering and automation from Central South University, Changsha, China, in 2014, where he is currently working toward the Ph.D. degree in electrical engineering.

His research interests include matrix converters and wireless power transfer.

0278-0046 (c) 2018 IEEE. Personal use is permitted, but republication/redistribution requires IEEE permission. See http://www.ieee.org/publications_standards/publications/rights/index.html for more information.